ELECTROCHEMISTRY

Ultralong cycle stability of aqueous zinc-ion batteries with zinc vanadium oxide cathodes

Lulu Wang[1], Kuo-Wei Huang[2], Jitao Chen[1]*, Junrong Zheng[1]*

Rechargeable aqueous zinc-ion batteries are promising candidates for large-scale energy storage but are plagued by the lack of cathode materials with both excellent rate capability and adequate cycle life span. We overcome this barrier by designing a novel hierarchically porous structure of Zn-vanadium oxide material. This $Zn_{0.3}V_2O_5{\cdot}1.5H_2O$ cathode delivers a high specific capacity of 426 mA·h g^{-1} at 0.2 A g^{-1} and exhibits an unprecedented superlong-term cyclic stability with a capacity retention of 96% over 20,000 cycles at 10 A g^{-1}. Its electrochemical mechanism is elucidated. The lattice contraction induced by zinc intercalation and the expansion caused by hydronium intercalation cancel each other and allow the lattice to remain constant during charge/discharge, favoring cyclic stability. The hierarchically porous structure provides abundant contact with electrolyte, shortens ion diffusion path, and provides cushion for relieving strain generated during electrochemical processes, facilitating both fast kinetics and long-term stability.

INTRODUCTION

Lithium-ion batteries dominate the present electrochemical energy storage landscape (*1*, *2*), but their environmental impact and safety hazard have limited their large-scale deployment (*3*–*5*). In this regard, rechargeable aqueous batteries using water-based electrolytes with good safety, facile assembly, and environmental benignity are promising alternatives for grid-scale electrochemical energy storage. Furthermore, aqueous electrolytes offer a higher ionic conductivities (ca. 1 S cm^{-1}) by three orders of magnitude than organic electrolytes (ca. 1 to 10 mS cm^{-1}), favoring high-rate capabilities (*6*).

In particular, aqueous zinc-ion batteries (ZIBs) outperform others owing to the properties of Zn anodes, including low-cost stemming from high abundance and large-scale production (*7*, *8*), nontoxicity (*8*), high capacity (820 mA·h g^{-1}) (*7*), relatively low redox potential (−0.76 V versus standard hydrogen electrode) (*9*, *10*), and considerable electrochemical stability in water due to a high over potential for hydrogen evolution (*8*, *11*). Moreover, ZIBs operate through a multiple-electron transfer, rendering higher storage capacity compared to Li- or Na-ion batteries (*12*, *13*). Alkaline Zn/MnO_2 batteries have been explored to reversibly access the full two-electron capacity (617 mA·h g^{-1}) of MnO_2 for extended cycles recently (*14*–*17*), although the KOH-based electrolyte, in general, would lead to poor recharge ability due to the formation of irreversible by-products and zinc dendrite, which is subject to a number of parameters, such as current density and substrate type (*18*). Recently developed, environment-friendly, and mild acidic electrolytes [e.g., 1 M $ZnSO_4$ (pH ~4.0)] were reported to remarkably improve the reversibility of the metallic Zn electrode (*6*, *19*).

However, cathode materials with both high capacity and good cycling performance remain a great challenge due to the high polarization of bivalent Zn^{2+} (*19*). Prussian blue analogs deliver limited capacity (~50 mA·h g^{-1}) (*10*, *20*–*22*), while manganese oxides, including α-, β-, γ-, δ-, and λ-MnO_2 suffer fast capacity fading (*9*, *12*, *23*–*28*). Although the cycling stability of Zn/MnO_2 batteries is significantly improved by introducing a $MnSO_4$ additive in the $ZnSO_4$ aqueous electrolyte to suppress the dissolution of Mn^{2+} during cycling, the rate capability of ZIBs still cannot meet the expectation of practical applications (*19*). High natural abundance, low cost, and multiple oxidation states of vanadium motivate the exploration of vanadium-based compounds as cathode materials for ZIBs (*29*–*32*). Recently, layered metal vanadates ($A_xV_mO_n$, A = metal cations) with open framework crystal structure have been applied to aqueous ZIBs (*6*, *33*–*36*), where metal cations embedded in the V_mO_n layers act as strong pillars to provide expanded interlayer spacing for reversible Zn^{2+} intercalation/deintercalation, thereby ensuring fast and reversible Zn^{2+} intercalation/deintercalation. In previous studies, a wide variety of nanostructured metal vanadates, including zero-dimensional (0D) nanoparticles, 1D nanowires/nanobelts/nanorods, and 2D nanoflakes, have been fabricated for ZIBs. For instance, Nazar and colleagues (*6*) presented a bilayered $Zn_{0.25}V_2O_5{\cdot}nH_2O$ nanobelts cathode, which delivered a capacity of 300 mA·h g^{-1} at 50 mA g^{-1} and retained 80% capacity after 1000 cycles. The (001) interlayer distance sharply decreases by 2.4 Å due to the intercalation of Zn^{2+} and expulsion of water from the interlayer during discharge. Kim and colleagues (*34*) fabricated $Na_2V_6O_{16}{\cdot}3H_2O$ nanorods with a high specific capacity of 361 mA·h g^{-1} and 80% capacity maintained over 1000 cycles. Similar to many other battery electrode materials, these cathodes suffer from either repeated lattice expansion/contraction or strains generated from Zn^{2+} insertion/extraction during charge/discharge processes, resulting in structure failure and unsatisfactory cyclic stability.

Here, we design a novel ZIB cathode material, hierarchically porous $Zn_{0.3}V_2O_5{\cdot}1.5H_2O$ (ZVO) nanoflowers by spontaneous phase transition from VOOH hollow nanospheres during electrochemical cycling in 3 M $Zn(CF_3SO_3)_2$ electrolyte, following the general guiding principles: (i) The large surface area of the hierarchically porous morphology provides abundant contact between electrode and electrolyte and short Zn^{2+} diffusion path, leading to high-rate capability (*37*, *38*); (ii) the porous structure renders facile alleviation for the strains arising from Zn^{2+} and H^+ insertion/extraction, extending cycle life of the batteries (*39*–*41*); and (iii) the impact of charge/discharge on the host lattice structure is minimized by the coinsertion of Zn^{2+}/H^+ ions. The cathode delivers a high capacity of 426 mA·h g^{-1} at 0.2 A g^{-1} and an unprecedented ultralong cycle life is achieved over 20,000 cycles with 96% capacity retention at 10 A g^{-1}. The morphological and structural evolution of cathode and the energy storage mechanism are elucidated by means of ex situ x-ray diffraction (XRD), ex situ x-ray photoelectron spectroscopy (XPS), scanning/transmission electron microscopy (SEM/TEM),

[1]College of Chemistry and Molecular Engineering, Beijing National Laboratory for Molecular Sciences, Peking University, Beijing 100871, China. [2]KAUST Catalysis Center and Division of Physical Science and Engineering, King Abdullah University of Science and Technology, Thuwal 23955-6900, Saudi Arabia.
*Corresponding author. Email: junrong@pku.edu.cn (J.Z.); chenjitao@pku.edu.cn (J.C.)

and scanning TEM/energy dispersive spectroscopy (STEM-EDS) mapping combined with electrochemical measurements.

RESULTS AND DISCUSSION

Electrochemical phase transformation

The VOOH sample is synthesized by a hydrothermal method (*42*). The XRD pattern of the sample (Fig. 1A) presents several weak diffraction peaks. These peaks match well with the (020), (120), (031), (131), and (200) crystalline planes of lepidocrocite VOOH (*42*, *43*), which has an analogous crystal structure to the orthorhombic γ-FeOOH (Joint Committee on Powder Diffraction Standards card no. 74-1877). The SEM image (Fig. 1B) shows a nanosphere shape with considerably rough surface. The sphere diameter ranges from 100 to 300 nm. TEM images (Fig. 1C) show a sharp contrast between the dark edge and pale center, verifying the hollow interior of the spheres. The hollow spherical structure comprises densely packed particulate subunits, and the thickness of the shell reaches 40 nm on average, about fifth of the sphere diameter (Fig. 1D). The interplanar spacing of 0.21 nm can be observed in the high-resolution TEM image (Fig. 1E), corresponding to the (131) plane of L-VOOH. The selected area electron diffraction pattern (Fig. 1D, inset) can also be indexed as the orthorhombic L-VOOH. The energy dispersive x-ray spectroscopy (EDX) analysis (fig. S1) shows that V and O elements are distributed homogeneously with the ratio of about 1:2, in accordance with the stoichiometry of VOOH. We perform XPS to probe the oxidation state of vanadium and electronic environment of oxygen in the as-synthesized VOOH. The binding energies of V $2p_{3/2}$ and V $2p_{1/2}$ centered at 515.8 and 523.1 eV are in agreement with literature values for V^{3+} (Fig. 1F) (*43*). The XPS spectrum of the O 1s core level can be deconvoluted into three peaks situated at 529, 529.8, and 531.5 eV, attributed to the different forms of O^{2-} in V—O, O—H, and H_2O, respectively. The difference in binding energy between O 1s and V $2p_{3/2}$ is 13.5 eV, close to that of V^{3+} in previous reports (*44*).

The VOOH sample is electrochemically transformed into crystal water-containing structure in an aqueous electrolyte, investigated in coin cells using Zn foil anode, 3 M $Zn(CF_3SO_3)_2$ electrolyte, and glass fiber separator. When the cell is galvanostatically cycled at a rate of 0.2 A g^{-1}, the specific capacity increases continuously, reaching 426 mA·h g^{-1} after 10 cycles (Fig. 2A and fig. S2). Figure 2B shows the cyclic voltammetry (CV) curves of VOOH electrode at a scan rate of 0.2 mV s^{-1}. The initial cycle reveals one reduction peak at 0.75 V and three oxidation peaks at 1.01, 1.14, and 1.43 V, respectively. On consecutive cycles, the reduction peak at 0.75 V vanishes, and two reduction peaks emerge at 0.59 and 0.92 V. The oxidation peaks at 1.01 and 1.14 V shift to lower potential at 0.72 and 1.05 V, respectively, and the peak at 1.43 V disappears. The peak positions remain almost unchanged in subsequent cycles. The peak currents gradually increase in successive cycling due to the activation of cathode, accompanying the morphology change from nanospheres to nanoflowers (Fig. 3A).

The significant difference in peak positions between the initial and subsequent CV profiles indicates that an irreversible phase transition takes place during electrochemical cycling. The voltage profile in the first cycle is distinct in appearance from those in the subsequent cycles (Fig. 2A), demonstrating that the phase transition is most significant in the first cycle. We apply ex situ XRD measurements to explore the structural evolution of VOOH at the selected states during the first cycle and different cycling stages (Fig. 2, C and D). At point A (in Fig. 2A), the dominant XRD signals correspond to the $Zn_x(OTf)_y(OH)_{2x-y}{\cdot}nH_2O$ precipitation (*45*). We observe the flaky precipitate on the surface of nanospheres (fig. S3a), further confirming the formation of the $Zn_x(OTf)_y(OH)_{2x-y}{\cdot}nH_2O$ precipitation. $Zn_x(OTf)_y(OH)_{2x-y}{\cdot}nH_2O$ is the product of OH^- ions reacting with

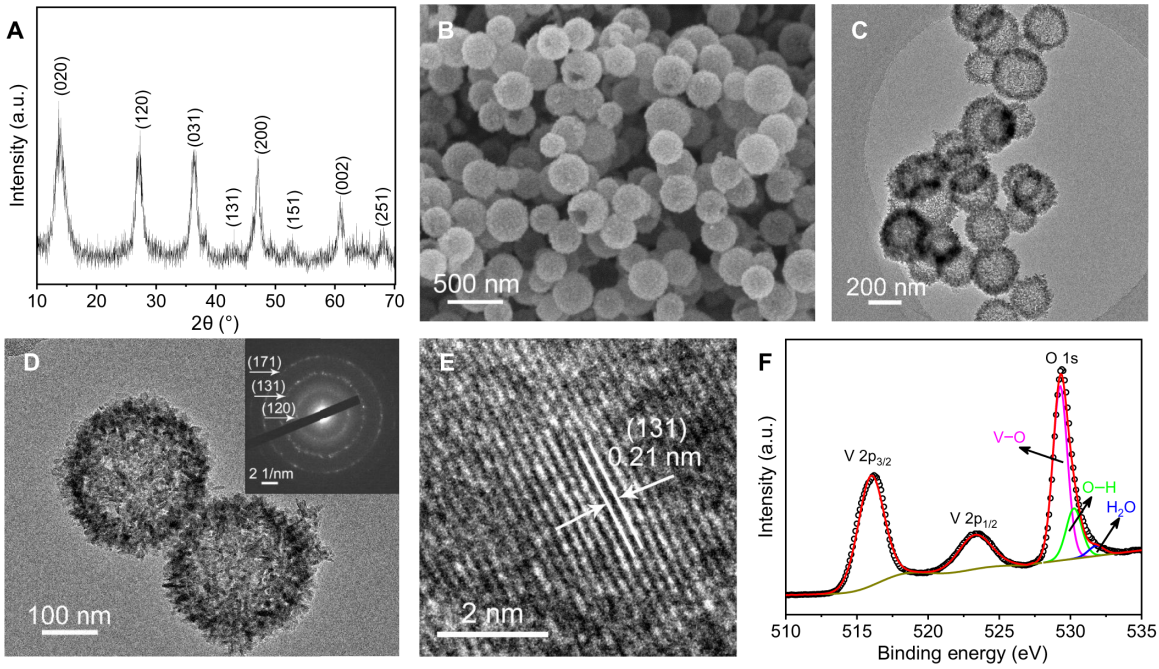

Fig. 1. Structural and morphological characterization of the VOOH nanospheres. (**A**) XRD pattern, (**B**) SEM image, (**C**) TEM image, (**D**) selected area electron diffraction, (**E**) high-resolution TEM image of the VOOH nanospheres, and (**F**) V 2p and O 1s XPS spectra. a.u., arbitrary units.

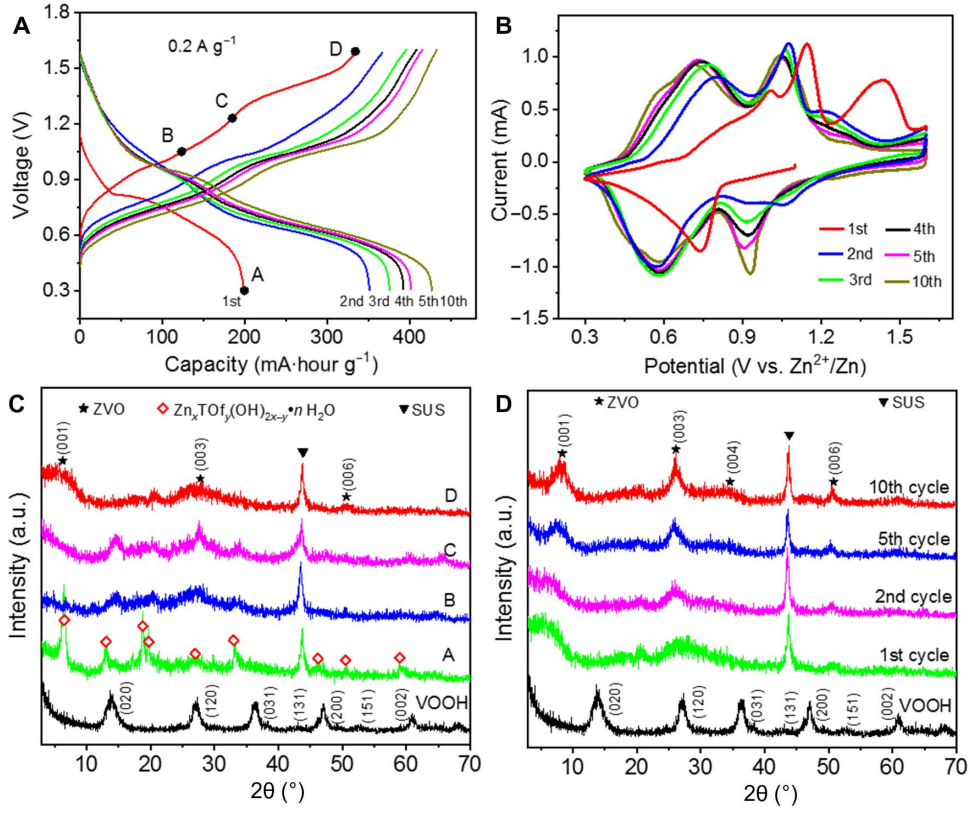

Fig. 2. Aqueous phase transition from VOOH nanospheres to hierarchically porous ZVO nanoflowers. (**A**) Typical charge/discharge profiles for the initial 10 cycles in 3 M $Zn(CF_3SO_3)_2$ aqueous electrolyte at a rate of 0.2 A g^{-1}. (**B**) CV curves of VOOH electrode at a scan rate of 0.2 mV s^{-1} in the voltage range of 0.3 to 1.6 V. (**C**) XRD patterns of VOOH electrode at selected states during the first cycle. (**D**) XRD patterns of VOOH electrode at different cycling stages. SUS, steel use stainless.

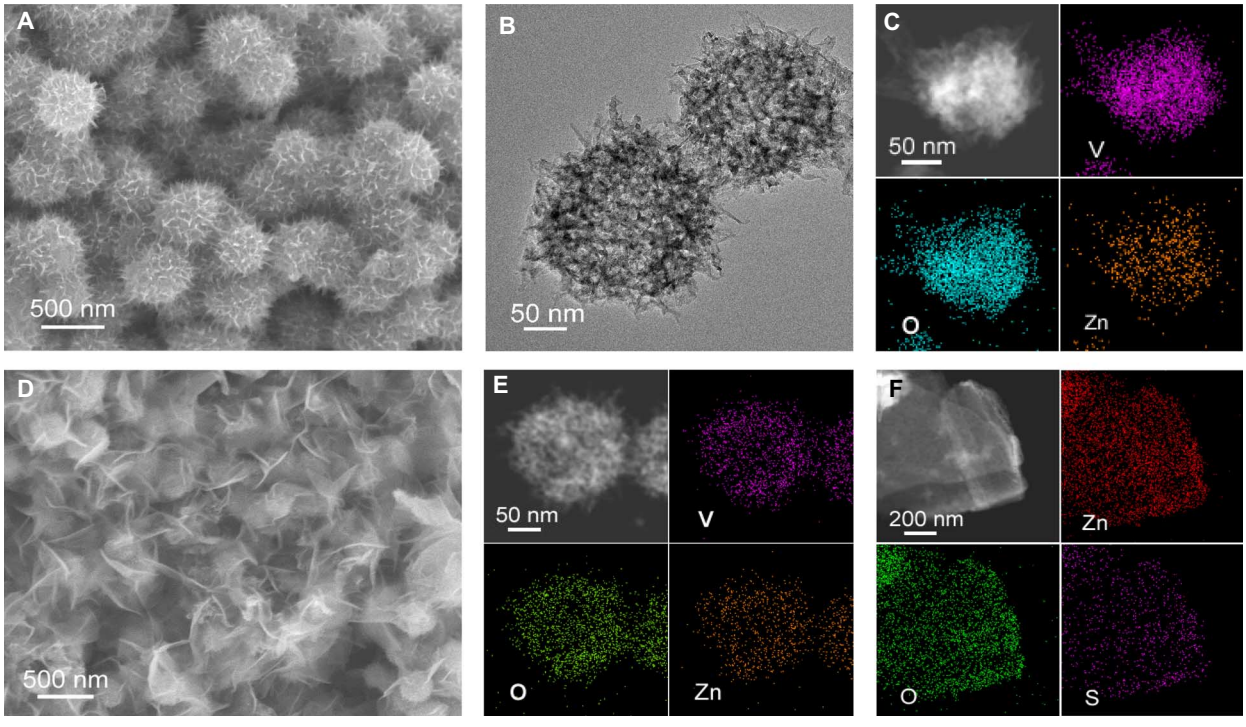

Fig. 3. Morphological and compositional characterization of the ZVO electrode during charge/discharge. (**A**) SEM image, (**B**) TEM image, and (**C**) STEM image and corresponding STEM-EDS elemental mapping images of the fully charged ZVO electrode. (**D**) SEM image and (**E** and **F**) STEM image and corresponding STEM-EDS elemental mapping images of the fully discharged ZVO electrode.

$Zn(CF_3SO_3)_2$ and H_2O in 3 M $Zn(CF_3SO_3)_2$ aqueous electrolyte. OH^- ions in the electrolyte come from the decomposition of water. As a consequence, equivalent amount of H^+ ions are produced. These H^+ cannot exist in the electrolyte by their own and must insert into the VOOH electrode to reach a neutral charge state during discharge. EDX mapping also shows that Zn element is uniformly distributed in the discharged nanospheres (fig. S4A). The results suggest that the reduction peak at 0.75 V represents the coinsertion of Zn^{2+}/H^+ into VOOH cathode. Upon charging to 1.2 V (A → C), the characteristic peaks for the flaky precipitation diminish to disappearance, and the number of flakes on nanospheres decreases gradually to zero (fig. S2, B and C), indicating the oxidation peak at 1.14 V along with a shoulder at 1.01 V corresponding to the extraction of Zn^{2+} and H^+ from the VOOH cathode. At the end of the first charge (point D), the morphology of the active material changes from independent nanospheres to interconnected nanoflowers (Fig. 3, A and D). The oxidation peak at 1.43 V (Fig. 2A) originates from H extraction and O insertion into the VOOH cathode, and atomic rearrangements as the V(III) state undergo oxidation to the V(V) state. With increasing cycle number, the XRD peaks assigned to VOOH gradually disappear, and new peaks at 8.2°, 26°, 34°, and 50.3° designated to reflections from the (001) to (005) crystallographic planes of $Zn_{0.25}V_2O_5{\cdot}nH_2O$ continuously grow (Fig. 2D). The structural change during aqueous phase transition from VOOH to $Zn_xV_2O_5{\cdot}nH_2O$ electrode is shown in fig. S5. In nonaqueous electrolytes [0.2 M $Zn(CF_3SO_3)_2$ in acetonitrile], VOOH cathode delivers a small capacity of 146 mA·h g^{-1} (fig. S6) and remains unchanged after 10 cycles (fig. S7). In contrast, $ZnSO_4$ and $Zn(CF_3SO_3)_2$ aqueous electrolytes can trigger phase transformation during electrochemical cycling (figs. S8 and S9), unveiling the crucial role of aqueous media for the phase transition.

After aqueous activation, the morphology of active material changes from the initial nanospheres to hierarchically porous nanoflowers consisting of interconnected nanosheets with a thickness of ~30 nm, as revealed in SEM (Fig. 3A) and TEM (Fig. 3B) images. According to the Brunauer-Emmett-Teller analysis, the specific surface area of the hierarchically porous ZVO nanoflowers is determined to be 33.5 m^2 g^{-1}, much larger than those of 1D V-based nanowire cathodes of ZIBs (H-NVO nanowire, 19.7 m^2 g^{-1}; NVO nanowire, 9.5 m^2 g^{-1}) (*35*). Nitrogen adsorption-desorption isotherm of the hierarchically ZVO nanoflowers (fig. S10) presents a typical type IV behavior with an H3 hysteresis, implying the presence of mesoporous structure. Meanwhile, the H3-type hysteresis demonstrates that the cathode has sheet-like structure, in agreement with the SEM and TEM images. The Barrett-Joyner-Halenda results (fig. S10, inset) reveal that the average pore size is 23.2 nm. The porous structure with large specific surface area can provide abundant contact between electrode and electrolyte, more active Zn storage sites and shorten the ion diffusion path, accounting for the fast electrochemical kinetics. Inductively coupled plasma optical emission spectroscopy (ICP-AES) (table S1) and quantitative STEM-EDS analysis (fig. S11a) both show the molar ratio of Zn to V in ZVO is 0.15. The crystalline water content can be determined by the weight loss in the temperature range of 150° to 350°C from the thermosgravimetric analysis (TGA) result. As shown in fig. S12, ~9.1% weight loss occurring until 150°C is mainly attributed to the physically absorbed water. Additional 12.1% weight loss of appearing from 150° to 350°C primarily corresponds to the loss of structural water (~340°C), equivalent to 1.5 molecule of water per formula unit. ICP-AES and TGA studies further confirm that the stoichiometric formula for the transformed hierarchical nanoflowers is ZVO.

Electrode reaction mechanism

To elucidate the storage mechanism of Zn/ZVO battery, we investigate the morphological and structural evolution of ZVO electrode during charge/discharge with field-emission scanning electron microscopy (FE-SEM), TEM, XRD, and XPS analyses. Fully discharged ZVO cathode is composed of nanoflowers and flaky precipitate, as shown in Fig. 3 (D to F). The successful zinc intercalation reaction in the cathode is validated by the quantitative STEM-EDS analysis of the ZVO cathode at fully discharged/charged states. The distribution of the elements in Fig. 3E demonstrates that the nanoflowers consist of V, O, and Zn. In contrast, Zn, O, and S are uniformly distributed in flaky precipitate with no signal of V (Fig. 3F). The Zn content increases by 0.75 per formula unit from the fully charged to the discharged ZVO nanoflowers (fig. S11, a and b). In addition, STEM-EDS mapping confirms that Zn is stored not only in the ZVO nanoflowers but also in the discharge-produced flake-like $Zn_x(OTf)_y(OH)_{2x-y}{\cdot}nH_2O$ precipitation (Fig. 3F), as evidenced by the XRD signal of fully discharged ZVO cathode in Fig. 4A. The insertion of H^+ into the ZVO cathode is further confirmed by the fact that the ZVO cathode delivers limited capacity and exhibits different charge/discharge profiles with larger over potential in organic Zn^{2+}-based electrolyte due to the absence of H^+ ions in organic electrolyte, whereas a much larger capacity and a long discharge plateau are observed after adding 1 weight % (wt %) H_2O in organic electrolyte (fig. S13A).

We carry out ex situ XRD measurements to investigate the structural evolution of ZVO electrode during the charge and discharge processes. Figure 4A shows the XRD pattern of ZVO electrode at different charge/discharge states at the current density of 0.2 A g^{-1}. New peaks located at 6.6°, 13.2°, 19.8°, 26.3°, 33.2°, 48.4°, and 59.2° emerge and gradually grow when discharged from 1.0 to 0.3 V, matching well with the pattern of $Zn_x(OTf)_y(OH)_{2x-y}{\cdot}nH_2O$. The structural evolution in subsequent charge process follows the reverse trend to that of discharge. Peaks assigned to $Zn_x(OTf)_y(OH)_{2x-y}{\cdot}nH_2O$ precipitation disappear with voltage reversal, indicating that the Zn^{2+} and H^+ intercalation/deintercalation through ZVO is highly reversible. The charge screening function of the cointercalated water in the redox reactions is reflected by the facilitated charge transfer in aqueous electrolyte, as evidenced by electrochemical impedance spectroscopy (EIS) analysis (fig. S14). Nyquist plot of in aqueous electrolyte shows smaller semicircle, demonstrating the relatively low interfacial charge transfer resistances for the cathodes in water containing solutions. The Rs (series resistance) and Rct (interfacial charge transfer resistance) values obtained from the fit are 1.5 and 11.4 ohms in the aqueous electrolyte, smaller than those in the organic electrolyte with adding 1 wt % H_2O (3.4 and 18.9 ohms) and organic electrolyte (10.3 and 60.1 ohms). In aqueous electrolytes, the decreased interfacial energy penalty at the cathode-electrolyte interface allows the ZVO cathode to achieve larger specific capacity (fig. S13A). Such a hydration effect that the charge screening of hydration can significantly decrease the Coulombic repulsion and the desolvation energy penalty at the interface has been revealed in recent studies (*46*, *47*). In addition, the ZVO cathode shows rapid capacity loss in organic Zn-ion electrolyte, whereas good cycling stability is observed in aqueous electrolyte (fig. S13B), suggesting that the crystal water residing in V_2O_5 interlayers probably serves as pillars to maintain the structural stability during the charge/discharge progress.

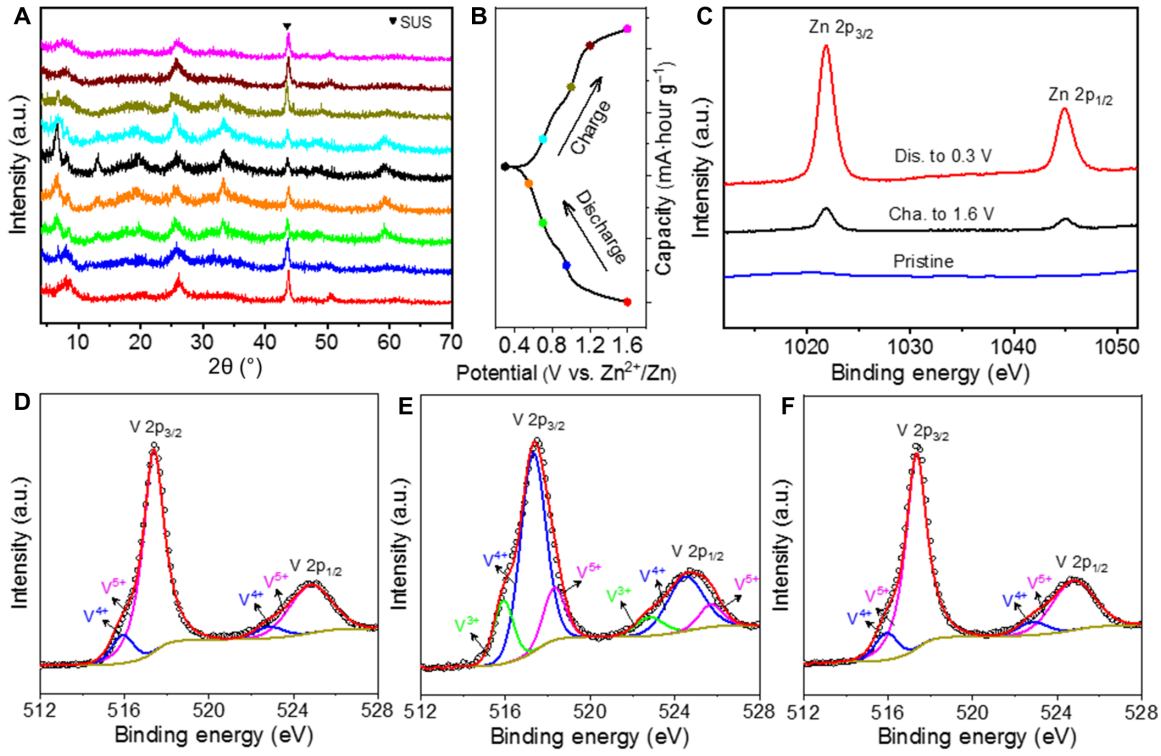

Fig. 4. Electrochemical mechanism studies. (**A**) Ex situ XRD patterns of the ZVO electrode at different charge/discharge states as indicated in (B). (**B**) Corresponding charge/discharge curves at 0.2 A g^{-1} in 3 M $Zn(CF_3SO_3)_2$ aqueous electrolyte. Ex situ high-resolution XPS spectra of the (**C**) Zn 2p region of pristine VOOH, fully discharged and charged ZVO electrodes. (**D** to **F**) V 2p region of pristine, fully discharged and charged ZVO electrodes.

We further perform the ex situ XPS analyses of cathode materials at original and fully discharged/charged states to explore the storage mechanism. As shown in Fig. 4C, no Zn signal can be detected in the initial state (blue line). At the fully charged state, two small Zn 2p core level peaks emerge, implying that a small amount of Zn^{2+} has been successfully preintercalated into the V_2O_5 interlayers after phase transition. When discharged to 0.3 V, the Zn 2p signals located at 1021.8 eV ($2p_{3/2}$) and 1044.9 eV ($2p_{1/2}$) increase substantially, caused by the intercalated Zn and the zinc hydroxide triflate precipitation.

Figure 4 (D to F) shows the high-resolution XPS spectrum of the V 2p. The V 2p spectra of the pristine ZVO cathode (Fig. 4D) can be deconvoluted into the V^{5+} signal ($2p_{3/2}$: 517.3 eV) accompanied by a weak V^{4+} component ($2p_{3/2}$: 515.8 eV). The V_2O_5 framework is partially reduced because of the existence of indigenous Zn^{2+} in the interlayers. At fully discharged state, V^{4+} signal ($2p_{3/2}$: 517.2 eV) is dominant, and a V^{3+} component ($2p_{3/2}$: 515.7 eV) emerges simultaneously (Fig. 4E). Upon charging, we recover the pristine V 2p spectrum (Fig. 4F), indicative of a reversible electrochemical redox of the V_2O_5 framework as a result of Zn^{2+}/H^+ intercalation.

We also examine the Zn anode to understand the high reversibility of the Zn/ZVO cell chemistry. After 20,000 cycles, we observe neither dendritic morphology (fig. S15) nor formation of by-products such as ZnO or $Zn(OH)_2$ (fig. S16), favoring the long-term cyclic stability of Zn/ZVO batteries.

The inserted Zn^{2+} and H^+ can be quantified by combining the quantitative STEM-EDS analysis with the electron transfer number during discharge. Elemental analysis from STEM-EDS analysis (fig. S11) shows that the molar ratio of Zn:V in ZVO nanoflower increases from 0.3:2 to 1.05:2 after full discharge. A high capacity of 426 mA·h g^{-1} is delivered at 0.2 A g^{-1}, corresponding to a ~2.67 electron redox process. The amount of inserted H^+ and Zn^{2+} in each ZVO formula unit is calculated to be 1.17 and 0.75, respectively. The insertion of H^+ and Zn^{2+} contributes to 44% (about 187 mA·h g^{-1}) and 56% (about 239 mA·h g^{-1}) capacity, respectively. The charge product is ZVO, and the corresponding discharge products are $H_{1.17}Zn_{1.05}V_2O_5{\cdot}1.5H_2O$ and $Zn_x(OTf)_y(OH)_{2x-y}{\cdot}nH_2O$. Thus, the electrochemical reactions of the rechargeable aqueous Zn/ZVO batteries can be formulated as below

$$\text{Cathode}: 1.17H_2O \leftrightarrow 1.17H^+ + 1.17OH^- \quad (1)$$

$$Zn_{0.3}V_2O_5{\cdot}1.5H_2O + 0.75Zn^{2+} + 1.17H^+ + 2.67e^- \leftrightarrow H_{1.17}Zn_{1.05}V_2O_5{\cdot}1.5H_2O \quad (2)$$

$$0.585Zn^{2+} + ay/2Zn(OTf)_2 + 1.17OH^- + anH_2O \leftrightarrow aZn_x(OTf)_y(OH)_{2x-y}{\cdot}nH_2O \quad (3)$$

$$(a(2x-y) = 1.17) \quad (4)$$

$$\text{Anode}: 1.335Zn \leftrightarrow 1.335Zn^{2+} + 2.67e^- \quad (5)$$

$$\text{Overall}: Zn_{0.3}V_2O_5{\cdot}1.5H_2O + ay/2Zn(OTf)_2 + (1.17+an)H_2O + 11.335Zn \leftrightarrow H_{1.17}Zn_{1.05}V_2O_5 1.5H_2O + aZn_x(OTf)_y(OH)_{2x-y}{\cdot}nH_2O \quad (6)$$

Electrochemical performance

Figure 5A shows the charge/discharge curves of the ZVO cathode at various current densities. The charge/discharge plateaus can be

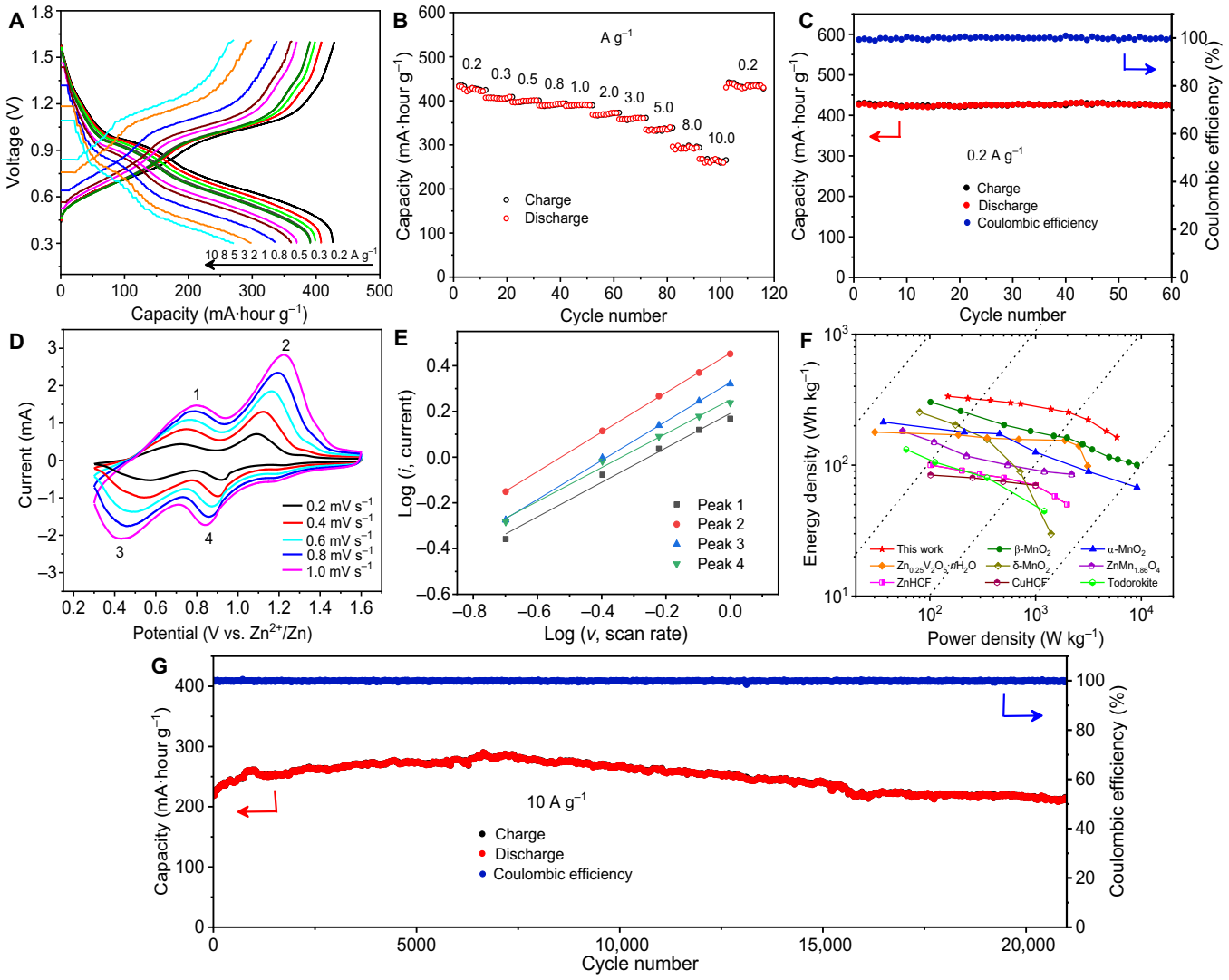

Fig. 5. Electrochemical behaviors of Zn/ZVO batteries with 3 M $Zn(CF_3SO_3)_2$ aqueous electrolyte. (**A**) Galvanostatic charge/discharge profiles for ZVO electrodes at various current densities. (**B**) Rate capability of ZVO electrodes. (**C**) Cycling performance at 0.2 A g^{-1}. (**D**) CV curves of ZVO electrodes at different scan rates. (**E**) Corresponding plots of log(*i*) versus log(*v*) at cathodic and anodic peaks. (**F**) Ragone plot of Zn/ZVO cell in comparison with other aqueous ZIBs. (**G**) Long-term cycling performance at 10 A g^{-1}.

easily discerned at the current density of 0.2 A g^{-1}, in accordance with the reduction/oxidation peaks of CV curves (Fig. 5D). The aqueous Zn/ZVO battery demonstrates superior rate capability, as shown in Fig. 5B. The discharge capacities are 426.3, 400.5, 388.8, 368.6, 334.5, and 265.2 mA·h g^{-1} at current densities of 0.2, 0.5, 1.0, 2.0, 5.0, and 10.0 A g^{-1}, respectively. Moreover, when the rate switched back to 0.2 A g^{-1}, a discharge capacity of 432.5 mA·h g^{-1} can be recovered, revealing excellent structural stability and a considerable tolerance to rapid Zn^{2+} (de)intercalation. At a low rate of 0.2 A g^{-1} (Fig. 5C), the ZVO cathode delivers a high discharge capacity of 426 mA·h g^{-1} and does not show any capacity decay after 60 cycles. The EIS plots at 1st, 5th, and 10th cycles charge almost overlap with each other (fig. S17), indicating that the impedance of the Zn/ZVO cell remains stable with the increasing cycles. In addition, the composition and concentration of electrolyte exert great influence on the electrochemical performance of the cell. Severe capacities decays are observed in diluted electrolytes [1 M $ZnSO_4$ and 1 M $Zn(CF_3SO_3)_2$] and can be alleviated by increasing the electrolyte concentration (figs. S8 and S9), which is attributed to the suppression of water activity and water-induced side reactions in high-concentration electrolyte. Furthermore, the concentrated 3 M $Zn(CF_3SO_3)_2$ electrolyte favors a larger specific capacity and a better cyclic stability than 3 M $ZnSO_4$ (figs. S8 to S9). The superior electrochemical properties in $Zn(CF_3SO_3)_2$ electrolyte is speculated to be due to the higher ionic conductivity of electrolyte (*48*) and facilitated charge transfer (fig. S18), which probably benefit from the smaller charge density (versus SO_4^{2-} with double charge) and weaker solvation effect of the bulky $CF_3SO_3^-$ anions (*49*).

Figure 5D shows the CV curves of the Zn/ZVO batteries measured at various sweep rates from 0.2 to 1.0 mV s^{-1} with a voltage window from 0.3 to 1.6 V. There are two distinct pairs of reduction/oxidation peaks located at around 0.59/0.70 and 0.93/1.05 V at a scanning rate of 0.2 mV s^{-1}, suggesting multistep intercalation/extraction processes. With continuous increase in the scan rates, the shapes of CV profiles remain similar except that the redox peaks slightly shift and gradually broaden. In principle, the power-law relationship between the peak current (*i*) and sweep rate (*v*) in a CV scan can be described by the following equation: $i = av^b$, where *a* and *b* are adjustable parameters.

The *b* value can reflect the rate-limiting step in the electrochemical process and varies in the range of 0.5 to 1.0. A *b* value of 0.5 indicates that the current is controlled by semi-infinite diffusion, while a *b* value of 1.0 suggests capacitive behavior (*50*). By fitting the plots of log(*i*) as a function of log(*v*) (Fig. 5E), the *b* values for peaks 1, 2, 3, and 4 are determined to be 0.75, 0.86, 0.85, and 0.74, respectively, indicating that the charge storage of ZVO is affected by both diffusion-controlled intercalation process and capacitor-like process. The capacitive contribution to capacity has been widely reported in V-based cathode materials for aqueous Zn-ion batteries (*31*, *33*). In addition, we use the galvanostatic intermittent titration technique (GITT) to estimate the Zn^{2+} ion diffusion coefficient in ZVO cathode (fig. S19). Despite its double valence, the GITT-determined Zn^{2+} ion diffusion coefficient is calculated to be 10^{-9} to 10^{-10} cm^2 s^{-1}, comparable with Zn^{2+} diffusion coefficient (10^{-8} to 10^{-9} cm^2 s^{-1}) in CVO cathode (*33*) and 10^2 to 10^4 higher than the Li^+ diffusion in $LiFePO_4$ (*51*) and $LiCoO_2$ (*52*) cathodes. The results indicate that the ZVO cathode has fast kinetics, favoring good rate capability. The high energy and high power densities of the Zn/ZVO battery are further confirmed by the Ragone plot (Fig. 4F). An energy density of 336 Wh kg^{-1} at a power density of 149 and 163 Wh kg^{-1} with a power density of 5.87 kW kg^{-1} (based on the mass of VOOH in cathode) can be simultaneously achieved, surpassing most of the previous reported Zn-ion batteries based on α-MnO_2 (*9*), β-MnO_2 (*48*), δ-MnO_2 (*23*), todorokite (*53*), $Zn_{1.86}Mn_2O_4$ (*49*), ZnHCF (*10*), CuHCF (*21*), VS_2 (*54*), $Zn_3V_2O_7(OH)_2$ (*50*), $Zn_{0.25}V_2O_5{\cdot}nH_2O$ (*6*), and $V_2O_5{\cdot}nH_2O$/GN (*55*) cathodes.

The most amazing property of the Zn/ZVO battery is its ultralong cyclic stability. The ZVO cathode retains a reversible capacity of 214 mA·h g^{-1} at 10.0 A g^{-1} (Fig. 5G) even after 20,000 cycles. The capacity retention is 96%, and the Coulombic efficiency maintains nearly 100%, superior to essentially all recently reported aqueous Zn-ion batteries that we are aware of (table S2). It is interesting that the specific capacity increases till about 5000th cycle and then fades slowly. The initial increase in the capacity is likely due to the gradual activation of the electrode. An increasing number of electrochemical sites are accessible on repeated cycling, thus leading to higher specific capacities. Moreover, with the increasing current density, the initial capacities increase, and greater and longer period of cycles is required for electrode activation (*34*, *56*). This trend can be observed in measurements with different current densities (2, 5, and 10 A g^{-1}; Fig. 5G and fig. S20) at all of which the long cycle stability is always observed. The reversible capacity of 316.4 mA·h g^{-1} after 1000 cycles is 90% of the initial value at the current density of 2 A g^{-1} (fig. S20a). When measured at 5 A g^{-1}, the ZVO delivers an initial discharge capacity of 318.4 mA·h g^{-1}, maintaining as high as 293.3 mA·h g^{-1} after 4000 cycles (fig. S20b). The Coulombic efficiency remains nearly 100%, and the capacity retention is 91%.

Mechanism of cycling stability

The unprecedented long cycling life of the battery at the high current density is the comprehensive result of a complex system, but two important factors may play critical roles. The first one is that the (001) interlayer distance of the ZVO barely changes during the charge/discharge processes, different from most other cathodes, as shown in Fig. 6 (A and B). The interlayer distance of ZVO at fully charged state is 10.8 Å and remains almost unchanged (within experimental uncertainty) with synchronous Zn^{2+}/H^+ intercalation after discharge. It is well known that the intercalation of zinc ions causes a lattice contraction due to the screening effect of interlayer electrostatic repulsion and the expulsion of water from the interlayers (*6*). In contrast, the intercalation of hydronium ions [to which the broad shoulder at 4.14 parts per million (ppm) of the red line in Fig. 6C likely belongs] results in lattice expansion (*45*). It is probably due to the cancelation of the two opposite effects that results in constant layer spacing during the charge/discharge cycles, minimizing the impact of electrochemical reactions that can lead to the instability of the cathode. The bi-ion insertion was also observed in another system with MnO_2 as cathode (*57*), but the process was stepwise and could not help maintain the lattice constant.

The hierarchical porous structure also favors the long-term cycling stability. Figure 6 (D to L) shows the morphology evolution of cathode during charge/discharge cycling. As discussed above, we convert the hollow spheres of VOOH (Fig. 6D) into hierarchically porous nanoflowers consisting of sphere-interconnected nanosheets (Fig. 6F) after a few cycles. The morphology only slightly changes up to 5000 cycles (Fig. 6, F to I). The hierarchical structure then gradually transforms into loosely packed nanoropes and nanorods (Fig. 6, J to L). Coincidently, the capacity also begins to drop (Fig. 5G), accompanying the gradual disappearance of the hierarchical structure. Despite the gradual morphology change after 5000 cycles, the ZVO electrode can still perfectly preserve its crystal structure (fig. S21). As shown in fig. S21, no obvious shift of (00 l) peak is observed even after 12,000 cycles at a high current density of 10 A g^{-1}, indicating that the interlayer spacing of ZVO electrode remains unchanged during cycling. In addition, probably because of the strain-friendly hierarchical morphology, the new structure can still attach to the current collector. Therefore, although the new structure cannot be as good as the hierarchically porous structure to provide more cushion for relieving the strain generated from the Zn^{2+} and H^+ insertion/extraction or to provide large surface area, they can still work as cathode material but with a smaller capacity and a shorter lifetime. This is a very likely reason responsible for the slow rather than abrupt capacity fading that accompanies the morphology change, which also contributes to the overall long cycling stability.

CONCLUSION

In summary, aqueous Zn/ZVO batteries composed of VOOH nanosphere cathode, 3 M $Zn(CF_3SO_3)_2$ electrolyte, and Zn anode are designed and fabricated. Upon cycling, VOOH hollow nanospheres undergo phase transition to form hierarchical ZVO nanoflowers. The hierarchical nanoflowers morphology provides abundant contact between electrode and electrolyte, as well as active Zn storage sites, facilitating fast electrochemical kinetics. On the other hand, preintercalated zinc ions and indigenous crystal water residing in interlayers serve as pillars and lubricant to stabilize the host structure, and the synchronous Zn^{2+}/H^+ ion insertion preserves the V_2O_5 interlayer spacing, favoring long-term cycling stability. As a result, the aqueous Zn/ZVO battery displays a high specific capacity of 426 mA·h g^{-1} at 0.2 A g^{-1}, a specific energy of ~268 Wh kg^{-1} at 1400 W kg^{-1} (cathode only), and a long-term cycling stability with 96% capacity retention after 20,000 cycles at 10 A g^{-1}. The combination of excellent electrochemical performance, good safety of aqueous electrolyte, low-cost electrode material without any active carbon support such as graphene and graphene oxide, and easy battery assembly makes the battery promising for grid-scale energy storage applications. The two principles, interlayer distance remaining constant and cushion space for relieving morphological strain, adopted in this work to improve the cyclic stability are expected to be general for many other battery material designs.

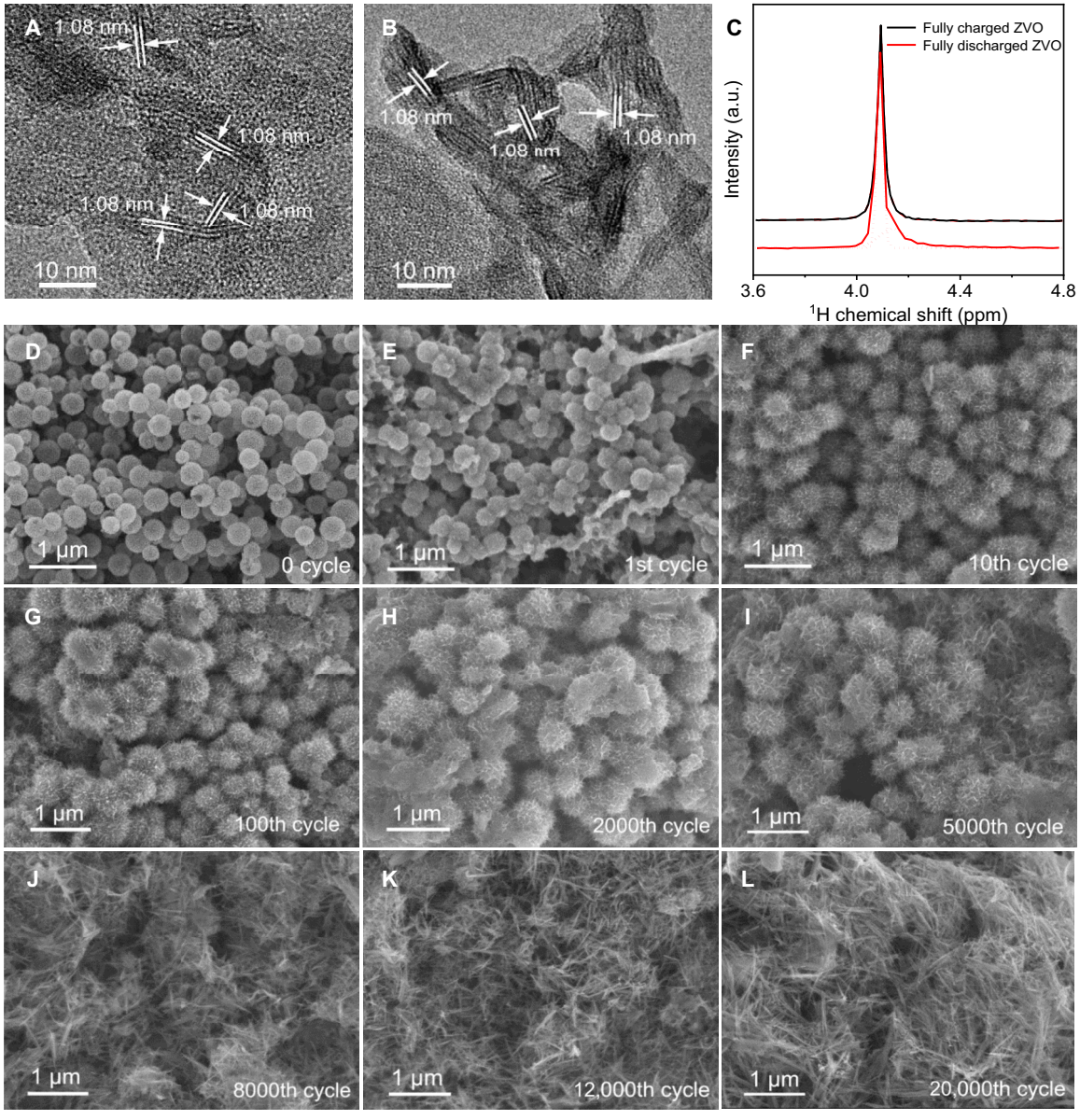

Fig. 6. Proof of excellent long-term cycling stability. Ex situ high-resolution TEM images of the ZVO electrode (**A**) at fully charged (1.6 V) and (**B**) discharged state (0.3 V). (**C**) Solid-state ^{1}H nuclear magnetic resonance (NMR) spectra of the fully charged and discharged ZVO electrode. The sharp peak at 4.09 ppm belongs to the structural water. The broad shoulder at 4.14 ppm in the fully discharged ZVO likely represents the hydronium. (**D** to **L**) SEM images of the cathode after *n*th cycles.

MATERIALS AND METHODS

Material preparation

Preparation of VOOH electrode

The VOOH nanospheres were synthesized by a hydrothermal reaction based on previous report with minor modification (*42*). In a typical synthesis, 2 mmol of NH_4VO_3 was dispersed into 45 ml of deionized water under stirring for 10 min to form a turbid solution. Then, 1 ml of 1 M HCl solution was added into the above solution at one drop per minute to obtain a transparent yellow solution, followed by the addition of 2 ml of $N_2H_4{\cdot}H_2O$. After stirring for 30 min at room temperature, the obtained gray suspension was transferred into a 50-ml Teflon-lined stainless steel autoclave and maintained at 160°C for 12 hours. Last, the product was centrifuged, washed with deionized water and ethanol several times, and dried in a vacuum at 70°C for 12 hours. The VOOH electrode was fabricated by mixing VOOH nanospheres, acetylene black, and polyvinylidene fluoride in *N*-methyl pyrrolidone in a 7:2:1 weight ratio. The slurry was then cast onto stainless steel (SUS 304) foil (round piece with a diameter of 14 mm and a thickness of ~25 μm) and vacuum-dried at 80°C for 12 hours. The loading mass of the active material in each electrode was ~2 mg cm^{-2} (~40 μm in thickness), corresponding to the areal capacity of ~0.85 mA·hour cm^{-2}.

Preparation of ZVO electrode

The ZVO electrode was prepared by aqueous electrochemical cycling in the CR2032-type coin cell with VOOH as the cathode, glass fiber membrane as the separator, and Zn metal foil as the anode in 3 M $Zn(CF_3SO_3)_2$ aqueous electrolyte. The cells were galvanostatically cycled at 0.2 A g^{-1} for 10 cycles. The as-obtained ZVO electrode was dried in vacuum oven at 80°C overnight.

Zn/ZVO batteries design

The Zn/ZVO aqueous batteries were assembled in the CR2032-type coin cell using the VOOH as the cathode, 3 M $Zn(CF_3SO_3)_2$ aqueous solution as the electrolyte, glass fiber membrane as the separator, and Zn metal foil as the anode, respectively. The typical weight of Zn foil was 23 mg cm^{-2}, and its thickness was ~30 μm (round piece of zinc with a diameter of 14 mm). For comparison, the Zn/ZVO nonaqueous batteries were assembled in the CR2032-type coin cell using the ZVO as the cathode, 0.2 M $Zn(CF_3SO_3)_2$ in acetonitrile with/without deionized water as the electrolyte, glass fiber membrane as the separator, and Zn metal plate as the anode, respectively.

Electrochemical measurements

Electrochemical performance was tested in CR2032-type coin cells assembled in air. CV measurements at various scan rates and EIS were conducted using a CHI760C electrochemical workstation. Galvanostatic charge/discharge and GITT measurements were executed on a LAND-CT2001A battery test system between 0.3 and 1.6 V. Calculation of current density and specific capacity were based on the mass of VOOH. Before the GITT measurement, the assembled cell was first charged and discharged at 20 mA g^{-1} for one cycle to stabilize the cells. The cell was charged/discharged at 50 mA g^{-1} for 0.5 hour, followed by relaxation for 1 hour to make the voltage reach the equilibrium. The procedure was repeatedly applied to the cell until the charge/discharge voltage reached 1.6/0.3 V.

Characterizations

The crystal structure of VOOH cathode was characterized by XRD (Rigaku D/Max-2400 diffractometer with Cu Kα radiation, 40 kV, 100 mA). The morphology analysis was carried out using a FE-SEM (S4800, Hitachi) and a TEM (JEM-2100F, JEOL) equipped with EDS for elemental analysis. The oxidation states of V in cathodes were examined using XPS (Axis Ultra, Kratos Analytical Ltd.). All XPS spectra were calibrated with respect to the C 1s peak binding energy of 284.8 eV. To investigate the water content, TGA (SDT Q600) was performed from room temperature to 360°C at a ramping rate of 10°C min^{-1} in nitrogen atmosphere. The specific surface areas and pore structures were obtained by N_2 adsorption-desorption measurement (ASAP 2020, Micrometrics). The molar ratio of Zn to V was measured using ICP-AES (Prodigy7, Leeman). The solid-state ^1H nuclear magnetic resonance (NMR) spectra were collected on a 400-MHz superconducting NMR spectrometer (Bruker Avance III).

SUPPLEMENTARY MATERIALS

Supplementary material for this article is available at http://advances.sciencemag.org/cgi/content/full/5/10/eaax4279/DC1

Fig. S1. EDS mapping and elemental analysis of the as-obtained VOOH.
Fig. S2. Discharge capacities of VOOH nanospheres in 3 M $Zn(CF_3SO_3)_2$ aqueous electrolyte at a rate of 0.2 A g^{-1}.
Fig. S3. Morphological evolution of the VOOH cathode during the first cycle in 3 M $Zn(CF_3SO_3)_2$ electrolyte at 0.2 A g^{-1}.
Fig. S4. EDS mapping and elemental analysis of the electrode after the first discharge.
Fig. S5. Schematic illustration of the aqueous phase transition from VOOH to ZVO electrode during electrochemical charge and discharge processes.
Fig. S6. Eletrochemical performance of VOOH electrodes in organic 0.2 M $Zn(CF_3SO_3)_2$/acetonitrile electrolyte at 0.2 A g^{-1}.
Fig. S7. XRD pattern and SEM image of the VOOH cathode after the electrochemical cycling in organic 0.2 M $Zn(CF_3SO_3)_2$/acetonitrile electrolyte.
Fig. S8. The cycling/electrochemical performance of Zn/VOOH cells in $ZnSO_4$ electrolyte with different concentrations (1 to 3 M) at 0.2 A g^{-1}.
Fig. S9. Comparison of the cycling/electrochemical performance of Zn/VOOH cells with different concentrations (1 to 3 M) of $Zn(CF_3SO_3)_2$ electrolyte at 0.2 A g^{-1}.
Fig. S10. Nitrogen adsorption-desorption isotherm and the Barrett-Joyner-Halenda pore size distribution plot of the hierarchical ZVO.
Fig. S11. TEM-EDS analysis of fully charged/discharged ZVO nanoflower cathode.
Fig. S12. TGA curve of the hierarchical ZVO nanoflowers under nitrogen atmosphere at a heat ramp of 10°C /min.
Fig. S13. Comparison of typical charge/discharge curves and cycling performance of ZVO electrodes in different electrolytes.
Fig. S14. Comparison of Nyquist plots of Zn/ZVO cells in different electrolytes.
Fig. S15. SEM images of the pristine and cycled Zn anode at 10 A g^{-1}.
Fig. S16. XRD patterns of the pristine and cycled Zn anodes.
Fig. S17. EIS spectra of Zn/ZVO cell after 1st, 5th, and 10th cycles at 0.2 A g^{-1} in 3 M $Zn(CF_3SO_3)_2$ aqueous electrolyte.
Fig. S18. Nyquist plots of Zn/ZVO cells at fully charged state in 3 M $ZnSO_4$ and 3 M $Zn(CF_3SO_3)_2$ electrolyte.
Fig. S19. Charge-discharge GITT profiles for the ZVO cathode and the corresponding Zn^{2+} diffusion coefficient (D).
Fig. S20. Long-term cycling performance of Zn/ZVO batteries at various current densities.
Fig. S21. Ex situ XRD patterns of the cycled ZVO electrode at 10 A g^{-1}.
Table S1. ICP-AES analysis of ZVO at fully charged state.
Table S2. Comparison of electrochemical performance of different cathode materials for aqueous Zn-ion batteries.

REFERENCES AND NOTES

1. D. Larcher, J. M. Tarascon, Towards greener and more sustainable batteries for electrical energy storage. *Nat. Chem.* **7**, 19–29 (2015).
2. Y. Lu, J. B. Goodenough, Y. Kim, Aqueous cathode for next-generation alkali-ion batteries. *J. Am. Chem. Soc.* **133**, 5756–5759 (2011).
3. J. B. Goodenough, Y. Kim, Challenges for rechargeable Li batteries. *Chem. Mater.* **22**, 587–603 (2010).
4. J. B. Goodenough, K. S. Park, The Li-ion rechargeable battery: A perspective. *J. Am. Chem. Soc.* **135**, 1167–1176 (2013).
5. J.-Y. Luo, Y.-Y. Xia, Aqueous lithium-ion battery $LiTi_2(PO_4)_3/LiMn_2O_4$ with high power and energy densities as well as superior cycling stability. *Adv. Funct. Mater.* **17**, 3877–3884 (2007).
6. D. Kundu, B. D. Adams, V. Duffort, S. H. Vajargah, L. F. Nazar, A high-capacity and long-life aqueous rechargeable zinc battery using a metal oxide intercalation cathode. *Nat. Energy* **1**, 16119 (2016).
7. J. F. Parker, C. N. Chervin, I. R. Pala, M. Machler, M. F. Burz, J. W. Long, D. R. Rolison, Rechargeable nickel-3D zinc batteries: An energy-dense, safer alternative to lithium-ion. *Science* **356**, 414–417 (2017).
8. X. G. Zhang, *Corrosion and Electrochemistry of Zinc* (Springer, 1996).
9. C. Xu, B. Li, H. Du, F. Kang, Energetic zinc ion chemistry: The rechargeable zinc ion battery. *Angew. Chem. Int. Ed.* **51**, 933–935 (2012).
10. L. Zhang, L. Chen, X. Zhou, Z. Liu, Towards high-voltage aqueous metal-ion batteries beyond 1.5 V: The zinc/zinc hexacyanoferrate system. *Adv. Energy Mater.* **5**, 1400930 (2015).
11. B. Dunn, H. Kamath, J.-M. Tarascon, Electrical energy storage for the grid: A battery of choices. *Science* **334**, 928–935 (2011).
12. M. H. Alfaruqi, V. Mathew, J. Gim, S. Kim, J. Song, J. P. Baboo, S. H. Choi, J. Kim, Electrochemically induced structural transformation in a γ-MnO_2 cathode of a high capacity zinc-ion battery system. *Chem. Mater.* **27**, 3609–3620 (2015).
13. D. E. Turney, J. W. Gallaway, G. G. Yadav, R. Ramirez, M. Nyce, S. Banerjee, Y.-c. K. Chen-Wiegart, J. Wang, M. J. D'Ambrose, S. Kolhekar, J. Huang, X. Wei, Rechargeable zinc alkaline anodes for long-cycle energy storage. *Chem. Mater.* **29**, 4819–4832 (2017).
14. G. G. Yadav, J. W. Gallaway, D. E. Turney, M. Nyce, J. Huang, X. Wei, S. Banerjee, Regenerable Cu-intercalated MnO_2 layered cathode for highly cyclable energy dense batteries. *Nat. Commun.* **8**, 14424 (2017).
15. G. G. Yadav, X. Wei, J. W. Gallaway, Z. Chaudhry, A. Shin, J. Huang, R. Yakobov, M. Nyce, N. Vanderklaauw, S. Banerjee, Rapid electrochemical synthesis of δ-MnO_2 from γ-MnO_2 and unleashing its performance as an energy dense electrode. *Mater. Today Energy* **6**, 198–210 (2017).
16. G. G. Yadav, X. Wei, J. Huang, J. W. Gallaway, D. E. Turney, M. Nyce, J. Secor, S. Banerjee, A conversion-based highly energy dense Cu^{2+} intercalated Bi-birnessite/Zn alkaline battery. *J. Mater. Chem. A* **5**, 15845–15854 (2017).
17. G. G. Yadav, X. Wei, J. Huang, D. Turney, M. Nyce, S. Banerjee, Accessing the second electron capacity of MnO_2 by exploring complexation and intercalation reactions in energy dense alkaline batteries. *Int. J. Hydrog. Energy* **43**, 8480–8487 (2018).
18. X. Wei, D. Desai, G. G. Yadav, D. E. Turney, A. Couzis, S. Banerjee, Impact of anode substrates on electrodeposited zinc over cycling in zinc-anode rechargeable alkaline batteries. *Electrochim. Acta* **212**, 603–613 (2016).

19. H. Pan, Y. Shao, P. Yan, Y. Cheng, K. S. Han, Z. Nie, C. Wang, J. Yang, X. Li, P. Bhattacharya, K. T. Mueller, J. Liu, Reversible aqueous zinc/manganese oxide energy storage from conversion reactions. *Nat. Energy* **1**, 16039 (2016).
20. L. Zhang, L. Chen, X. Zhou, Z. Liu, Morphology-dependent electrochemical performance of zinc hexacyanoferrate cathode for zinc-ion battery. *Sci. Rep.* **5**, 18263 (2015).
21. R. Trocoli, F. La Mantia, An aqueous zinc-ion battery based on copper hexacyanoferrate. *ChemSusChem* **8**, 481–485 (2015).
22. T. Gupta, A. Kim, S. Phadke, S. Biswas, T. Luong, B. J. Hertzberg, M. Chamoun, K. Evans-Lutterodt, D. A. Steingart, Improving the cycle life of a high-rate, high-potential aqueous dual-ion battery using hyper-dendritic zinc and copper hexacyanoferrate. *J. Power Sources* **305**, 22–29 (2016).
23. M. H. Alfaruqi, J. Gim, S. Kim, J. Song, D. T. Pham, J. Jo, Z. Xiu, V. Mathew, J. Kim, A layered δ-MnO_2 nanoflake cathode with high zinc-storage capacities for eco-friendly battery applications. *Electrochem. Commun.* **60**, 121–125 (2015).
24. B. Lee, H. R. Lee, H. Kim, K. Y. Chung, B. W. Cho, S. H. Oh, Elucidating the intercalation mechanism of zinc ions into alpha-mno2 for rechargeable zinc batteries. *Chem. Commun.* **51**, 9265–9268 (2015).
25. C. Yuan, Y. Zhang, Y. Pan, X. Liu, G. Wang, D. Cao, Investigation of the intercalation of polyvalent cations (Mg^{2+}, Zn^{2+}) into λ-MnO_2 for rechargeable aqueous battery. *Electrochim. Acta* **116**, 404–412 (2014).
26. B. Jiang, C. Xu, C. Wu, L. Dong, J. Li, F. Kang, Manganese sesquioxide as cathode material for multivalent zinc ion battery with high capacity and long cycle life. *Electrochim. Acta* **229**, 422–428 (2017).
27. B. Lee, C. S. Yoon, H. R. Lee, K. Y. Chung, B. W. Cho, S. H. Oh, Electrochemically-induced reversible transition from the tunneled to layered polymorphs of manganese dioxide. *Sci. Rep.* **4**, 6066 (2014).
28. C. Wei, C. Xu, B. Li, H. Du, F. Kang, Preparation and characterization of manganese dioxides with nano-sized tunnel structures for zinc ion storage. *J. Phys. Chem. Solids* **73**, 1487–1491 (2012).
29. G. Li, Z. Yang, Y. Jiang, W. Zhang, Y. Huang, Hybrid aqueous battery based on $Na_3V_2(PO_4)_3$/C cathode and zinc anode for potential large-scale energy storage. *J. Power Sources* **308**, 52–57 (2016).
30. P. He, Y. Quan, X. Xu, M. Yan, W. Yang, Q. An, L. He, L. Mai, High-performance aqueous zinc-ion battery based on layered $H_2V_3O_8$ nanowire cathode. *Small* **13**, 1702551 (2017).
31. N. Zhang, Y. Dong, M. Jia, X. Bian, Y. Wang, M. Qiu, J. Xu, Y. Liu, L. Jiao, F. Cheng, Rechargeable aqueous Zn–V_2O_5 battery with high energy density and long cycle life. *ACS Energy Lett.* **3**, 1366–1372 (2018).
32. M. H. Alfaruqi, V. Mathew, J. Song, S. Kim, S. Islam, D. T. Pham, J. Jo, S. Kim, J. P. Baboo, Z. Xiu, K.-S. Lee, Y.-K. Sun, J. Kim, Electrochemical zinc intercalation in lithium vanadium oxide: A high-capacity zinc-ion battery cathode. *Chem. Mater.* **29**, 1684–1694 (2017).
33. C. Xia, J. Guo, P. Li, X. Zhang, H. N. Alshareef, Highly stable aqueous zinc-ion storage using a layered calcium vanadium oxide bronze cathode. *Angew. Chem. Int. Ed.* **57**, 3943–3948 (2018).
34. V. Soundharrajan, B. Sambandam, S. Kim, M. H. Alfaruqi, D. Y. Putro, J. Jo, S. Kim, V. Mathew, Y.-K. Sun, J. Kim, $Na_2V_6O_{16}{\cdot}3H_2O$ barnesite nanorod: An open door to display a stable and high energy for aqueous rechargeable zn-ion batteries as cathodes. *Nano Lett.* **18**, 2402–2410 (2018).
35. P. Hu, T. Zhu, X. Wang, X. Wei, M. Yan, J. Li, W. Luo, W. Yang, W. Zhang, L. Zhou, Z. Zhou, L. Mai, Highly durable $Na_2V_6O_{16}{\cdot}1.63H_2O$ nanowire cathode for aqueous zinc-ion battery. *Nano Lett.* **18**, 1758–1763 (2018).
36. Y. Yang, Y. Tang, G. Fang, L. Shan, J. Guo, W. Zhang, C. Wang, L. Wang, J. Zhou, S. Liang, Li^+ intercalated $V_2O_5{\cdot}nH_2O$ with enlarged layer spacing and fast ion diffusion as an aqueous zinc-ion battery cathode. *Energy Environ. Sci.* **11**, 3157–3162 (2018).
37. J. Jiang, J. Liu, W. Zhou, J. Zhu, X. Huang, X. Qi, H. Zhang, T. Yu, CNT/Ni hybrid nanostructured arrays: Synthesis and application as high-performance electrode materials for pseudocapacitors. *Energy Environ. Sci.* **4**, 5000–5007 (2011).
38. H. Zhang, G. Cao, Z. Wang, Y. Yang, Z. Shi, Z. Gu, Growth of manganese oxide nanoflowers on vertically-aligned carbon nanotube arrays for high-rate electrochemical capacitive energy storage. *Nano Lett.* **8**, 2664–2668 (2018).
39. Q. An, Q. Wei, P. Zhang, J. Sheng, K. M. Hercule, F. Lv, Q. Wang, X. Wei, L. Mai, Three-dimensional interconnected vanadium pentoxide nanonetwork cathode for high-rate long-life lithium batteries. *Small* **11**, 2654–2660 (2015).
40. Y. Yao, M. T. McDowell, I. Ryu, H. Wu, N. Liu, L. Hu, W. D. Nix, Y. Cui, Interconnected silicon hollow nanospheres for lithium-ion battery anodes with long cycle life. *Nano Lett.* **11**, 2949–2954 (2011).
41. Q. Wei, Q. An, D. Chen, L. Mai, S. Chen, Y. Zhao, K. M. Hercule, L. Xu, A. Minhas-Khan, Q. Zhang, One-pot synthesized bicontinuous hierarchical $Li_3V_2(PO_4)_3$/C mesoporous nanowires for high-rate and ultralong-life lithium-ion batteries. *Nano Lett.* **14**, 1042–1048 (2014).
42. C. Wu, X. Zhang, B. Ning, J. Yang, Y. Xie, Shape evolution of new-phased lepidocrocite VOOH from single-shelled to double-shelled hollow nanospheres on the basis of programmed reaction-temperature strategy. *Inorg. Chem.* **48**, 6044–6054 (2009).
43. C. Z. Wu, Y. Xie, L. Y. Lei, S. Q. Hu, C. Z. OuYang, Synthesis of new-phased VOOH hollow "dandelions" and their application in lithium-ion batteries. *Adv. Mater.* **18**, 1727–1732 (2006).
44. H. Shi, H. Liang, F. Ming, Z. Wang, Efficient overall water-splitting electrocatalysis using lepidocrocite VOOH hollow nanospheres. *Angew. Chem. Int. Ed.* **56**, 573–577 (2017).
45. P. Oberholzer, E. Tervoort, A. Bouzid, A. Pasquarello, D. Kundu, Oxide vs. non-oxide cathode materials for aqueous zn batteries: An insight into the charge storage mechanism and consequences thereof. *ACS Appl. Mater. Interfaces* **11**, 674–682 (2019).
46. K. W. Nam, S. Kim, S. Lee, M. Salama, I. Shterenberg, Y. Gofer, J. S. Kim, E. Yang, C. S. Park, J.-S. Kim, S.-S. Lee, W.-S. Chang, S.-G. Doo, Y. N. Jo, Y. Jung, D. Aurbach, J. W. Choi, The high performance of crystal water containing manganese birnessite cathodes for magnesium batteries. *Nano Lett.* **15**, 4071–4079 (2015).
47. Y. Mizuno, M. Okubo, E. Hosono, T. Kudo, H. Zhou, K. Oh-ishi, Suppressed activation energy for interfacial charge transfer of a prussian blue analog thin film electrode with hydrated ions (Li^+, Na^+, and Mg^{2+}). *J. Phys. Chem. C* **117**, 10877–10882 (2013).
48. N. Zhang, F. Cheng, Y. Liu, Q. Zhao, K. Lei, C. Chen, X. Liu, J. Chen, Cation-deficient spinel $ZnMn_2O_4$ cathode in $Zn(CF_3SO_3)_2$ electrolyte for rechargeable aqueous zn-ion battery. *J. Am. Chem. Soc.* **138**, 12894–12901 (2016).
49. N. Zhang, F. Cheng, J. Liu, L. Wang, X. Long, X. Liu, F. Li, J. Chen, Rechargeable aqueous zinc-manganese dioxide batteries with high energy and power densities. *Nat. Commun.* **8**, 405 (2017).
50. C. Xia, J. Guo, Y. Lei, H. Liang, C. Zhao, H. N. Alshareef, Rechargeable aqueous zinc-ion battery based on porous framework zinc pyrovanadate intercalation cathode. *Adv. Mater.* **30**, 1705580 (2018).
51. Y. J. Zhu, C. S. Wang, Galvanostatic intermittent titration technique for phase-transformation electrodes. *J. Phys. Chem. C* **114**, 2830–2841 (2010).
52. M. Park, X. Zhang, M. Chung, G. B. Less, A. M. Sastry, A review of conduction phenomena in Li-ion batteries. *J. Power Sources* **195**, 7904–7929 (2010).
53. J. Lee, J. B. Ju, W. I. Cho, B. W. Cho, S. H. Oh, Todorokite-type MnO_2 as a zinc-ion intercalating material. *Electrochim. Acta* **112**, 138–143 (2013).
54. P. He, M. Yan, G. Zhang, R. Sun, L. Chen, Q. An, L. Mai, Layered VS_2 nanosheet-based aqueous zn ion battery cathode. *Adv. Energy Mater.* **7**, 1601920 (2017).
55. M. Yan, P. He, Y. Chen, S. Wang, Q. Wei, K. Zhao, X. Xu, Q. An, Y. Shuang, Y. Shao, K. T. Mueller, L. Mai, J. Liu, J. Yang, Water-lubricated intercalation in $V_2O_5{\cdot}nH_2O$ for high-capacity and high-rate aqueous rechargeable zinc batteries. *Adv. Mater.* **30**, 1703725 (2018).
56. P. He, G. Zhang, X. Liao, M. Yan, X. Xu, Q. An, J. Liu, L. Mai, Sodium ion stabilized vanadium oxide nanowire cathode for high-performance zinc-ion batteries. *Adv. Energy Mater.* **8**, 1702463 (2018).
57. W. Sun, F. Wang, S. Hou, C. Yang, X. Fan, Z. Ma, T. Gao, F. Han, R. Hu, M. Zhu, C. Wang, Zn/MnO_2 battery chemistry with H^+ and Zn^{2+} coinsertion. *J. Am. Chem. Soc.* **139**, 9775–9778 (2017).

Acknowledgments

Funding: We acknowledge financial support from the National Science Foundation of China (NSFC-21627805, 21673004, and 21821004) and MOST (2017YFA0204702) China. **Author contributions:** L.W. and J.Z. designed experiments. J.Z. supervised the project. L.W. and K.-W.H. performed experiments. All authors discussed experiments and results. L.W., J.C., and J.Z. prepared and revised the manuscript. **Competing interests:** The authors declare that they have no competing interests. **Data and materials availability:** All data needed to evaluate the conclusions in the paper are present in the paper and/or the Supplementary Materials. Additional data related to this paper may be requested from the authors.

Submitted 22 March 2019
Accepted 9 September 2019
Published 4 October 2019
10.1126/sciadv.aax4279

Citation: L. Wang, K.-W. Huang, J. Chen, J. Zheng, Ultralong cycle stability of aqueous zinc-ion batteries with zinc vanadium oxide cathodes. *Sci. Adv.* **5**, eaax4279 (2019).

ScienceAdvances

Ultralong cycle stability of aqueous zinc-ion batteries with zinc vanadium oxide cathodes

Lulu WangKuo-Wei HuangJitao ChenJunrong Zheng

Sci. Adv., 5 (10), eaax4279. • DOI: 10.1126/sciadv.aax4279

Science Advances (ISSN 2375-2548) is published by the American Association for the Advancement of Science. 1200 New York Avenue NW, Washington, DC 20005. The title *Science Advances* is a registered trademark of AAAS.